Two Higher-Order Shell Finite Elements with Stabilization Matrix

J. J. Rhiu,* R. M. Russell,† and S. W. Lee‡
University of Maryland, College Park, Maryland 20742

A 32-node three-dimensional solid element and a 16-node degenerate solid element that are applicable to analysis of thin-shell structural problems are presented in this paper. Both elements are formulated by using the Hellinger-Reissner principle with independent strain. The assumed independent strain field is divided into higher- and lower-order polynomial terms. The element stiffness matrix associated with the higher order assumed strain plays the role of the stabilization matrix. Various types of the higher-order assumed strain are tested for the present elements. The resulting finite-element models require much less time to compute the element stiffness matrix than the corresponding conventional mixed models or assumed displacement models with a full Gaussian quadrature rule. Numerical results demonstrate that, with a properly chosen set of higher-order assumed strain, the present elements produce reliable and very accurate solutions even for very thin plates and thin shells with deeply curved geometry.

I. Introduction

In recent years, considerable research has been devoted to developing the shell finite elements that are not subjected to the detrimental effect of locking and kinematic modes. One example is the reduced or selective integration technique. However, it has not always been successful in eliminating locking. Moreover, an excessively reduced integration may trigger spurious kinematic modes[1,2] and thus lead to a kinematically unstable finite-element model. Other examples are a stabilization matrix scheme to control the kinematic modes resulting from the use of a reduced integration,[3-5] the introduction of an assumed natural coordinate or covariant strain field,[6-9] a mode-decomposition approach,[10] and the hybrid/mixed formulation with either assumed strain or assumed stress.[11,12]

In 1978, Lee and Pian[13] presented a mixed formulation based on the Hellinger-Reissner principle with independent strain. In conjunction with the degenerate solid-shell element concept[14] and with a properly chosen assumed independent strain field, this method has generated effective and reliable finite-element models for linear or geometrically nonlinear analysis of thin-shell structures.[15-17] On the other hand, a three-dimensional solid element can be tailored for modeling of thin shells. Since the three-dimensional solid element does not directly include rotation degrees of freedom, it may be useful for solving nonlinear structural problems where a large rotational behavior is significant. Using the mixed formulation, an 18-node and a 32-node solid element tailored for thin-shell analysis were presented in Refs. 18 and 19. However, in the mixed formulation, it is necessary to invert a certain matrix to generate an element stiffness matrix. The size of this matrix is directly related to the number of assumed independent strain terms. Therefore, this formulation requires more time to create the element stiffness matrix of the same size than the assumed displacement model based on the principle of virtual work. This is a major drawback of the conventional mixed formulation.

In Ref. 20, a new mixed formulation also based on the Hellinger-Reissner principle with independent strain was proposed to overcome the drawback of the conventional mixed element. In this new mixed formulation, the assumed independent strain is divided into a higher-order component and a lower-order component. The lower-order assumed strain is substituted with the displacement-dependent strain evaluated at lower-order integration points. The higher-order assumed strain adopts a few higher-order polynomial terms, which are selected to suppress undesirable kinematic modes. By doing these, it is possible to make the new mixed formulation more efficient than the conventional mixed formulation. In addition, the new mixed formulation can provide a rational basis for introducing a stabilization matrix to element stiffness matrix. A 9-node and a 16-node degenerate solid shell element[21,22] and an 18-node three-dimensional solid element[23] were developed with the new mixed formulation.

In this paper, following the above new mixed formulation concept, a 32-node solid element is developed for the analysis of thin-shell structures. In addition, a 16-node degenerate solid-shell element is proposed with a set of assumed strain, which is different from the set examined in Ref. 22. Because of the higher-order deformation field assumption, these elements can represent shell behavior with high accuracy. The selection of the higher-order component of the assumed strain field is discussed in detail. Finally, the performance of these finite-element models is tested by solving several thin-plate and shell example problems.

II. Finite Element Formulation

Figures 1 and 2 illustrate a three-dimensional solid element with 32 nodes and the midsurface of a degenerate solid-shell element with 16 nodes. Local Cartesian coordinates x, y, and z, which are parallel to the orthogonal unit vectors $\boldsymbol{a}_1$, $\boldsymbol{a}_2$, and $\boldsymbol{a}_3$, respectively, are used to represent shell behavior as well as global Cartesian coordinates X, Y, and Z. The method of choosing these local coordinate unit vectors at integration points will be discussed later. In addition to these two coordinate systems, the parent or natural coordinate system with components ξ, η, and ζ, is used to describe the shell geometry and the kinematics of deformation. Note that the three-dimensional solid element has three degrees of freedom at each node. On the other hand, the degenerate solid-shell element needs three translational displacements and two rotational degrees of freedom at each node.

Received March 6, 1989; revision received Sept. 5, 1989.

*Research faculty, Department of Aerospace Engineering; currently at the Korea Aerospace Research Institute.
†Graduate student, Department of Aerospace Engineering.
‡Professor, Department of Aerospace Engineering. Member AIAA.

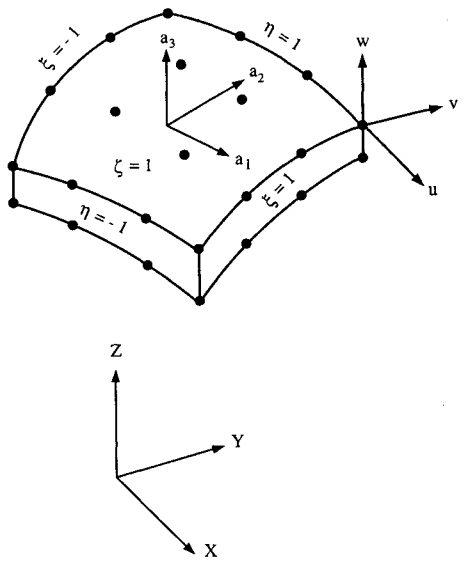

Fig. 1 A three-dimensional solid element with 32 nodes.

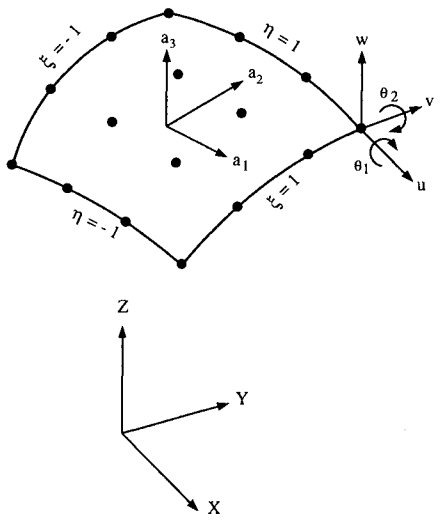

Fig. 2 The midsurface of a degenerate solid-shell element with 16 nodes.

The functional π_R for the Hellinger-Reissner principle is expressed as

$$\pi_R = \sum_e \int_e \left(\varepsilon^T C \bar{\varepsilon} - \frac{1}{2} \varepsilon^T C \varepsilon \right) dV_e - W \tag{1}$$

where the sign Σ indicates summation or assembly over all elements, V_e is the volume of element, W is the applied load term, and T represents transpose. For a solid element, the independent strain vector ε defined on the local coordinate system is

$$\varepsilon = \lfloor \varepsilon_{xx}, \varepsilon_{yy}, \varepsilon_{zz}, \varepsilon_{xy}, \varepsilon_{yz}, \varepsilon_{zx} \rfloor^T \tag{2}$$

In addition, the displacement-dependent local strain vector $\bar{\varepsilon}$ is expressed as

$$\bar{\varepsilon} = \lfloor \bar{\varepsilon}_{xx}, \bar{\varepsilon}_{yy}, \bar{\varepsilon}_{zz}, \bar{\varepsilon}_{xy}, \bar{\varepsilon}_{yz}, \bar{\varepsilon}_{zx} \rfloor^T \tag{3}$$

For a degenerate solid-shell element, the ε_{zz} and $\bar{\varepsilon}_{zz}$ terms do not appear in Eqs. (2) and (3). On the other hand, C in Eq. (1) is an elastic coefficient matrix. The stress-strain relationship for three-dimensional solids is modified to represent thin-shell behavior. As discussed in Ref. 23, this is done by ignoring the effect of normal stress σ_{zz} on ε_{xx} and ε_{yy}. Then, a modified 6×6 elastic coefficient matrix for the present three-dimensional solid element is expressed as follows:

$$C = \begin{bmatrix} \frac{E}{1-\nu^2} & \frac{\nu E}{1-\nu^2} & 0 & 0 & 0 & 0 \\ \frac{\nu E}{1-\nu^2} & \frac{E}{1-\nu^2} & 0 & 0 & 0 & 0 \\ 0 & 0 & E & 0 & 0 & 0 \\ 0 & 0 & 0 & G & 0 & 0 \\ 0 & 0 & 0 & 0 & \beta G & 0 \\ 0 & 0 & 0 & 0 & 0 & \beta G \end{bmatrix} \tag{4}$$

where E is Young's modulus, ν is Poisson's ratio, G is the shear modulus, and $\beta (= 5/6)$ is the transverse shear correction factor. For a degenerate solid-shell element, the 5×5 elastic coefficient matrix is obtained by deleting the third column and the third row in the above expression.

Symbolically, the displacement-dependent local strain vector $\bar{\varepsilon}$ in Eq. (3) can be expressed in terms of the element nodal degrees-of-freedom vector q_e as follows:

$$\bar{\varepsilon} = B(\xi, \eta, \zeta) q_e \tag{5}$$

where B is a matrix relating $\bar{\varepsilon}$ to q_e.

In the conventional mixed formulation, ε in Eq. (2) is composed of polynomial terms in the parent coordinates ξ, η, and ζ. For example, the three-dimensional solid element with 32 nodes in Ref. 19 employed 116 terms for the assumed strain field. Then, a substantial computing time is required to generate the element stiffness matrix of this finite-element model because of the need to invert a matrix of size 116×116.

Following the approach used in Refs. 20–22, the independent local strain vector ε in the present formulation is divided into such that

$$\varepsilon = \varepsilon_L + \varepsilon_H \tag{6}$$

where ε_L is the independent local strain vector with lower-order polynomial terms in ξ, η, and ζ. On the other hand, ε_H is the higher-order component of the independent local strain vector. Substituting Eq. (6) into Eq. (1), the functional π_R becomes

$$\pi_R = \sum_e \left(\int_e \varepsilon_L^T C \bar{\varepsilon} \, dV_e - \frac{1}{2} \int_e \varepsilon_L^T C \varepsilon_L \, dV_e + \int_e \varepsilon_H^T C \bar{\varepsilon} \, dV_e - \int_e \varepsilon_H^T C \varepsilon_L \, dV_e - \frac{1}{2} \int_e \varepsilon_H^T C \varepsilon_H \, dV_e \right) - W \tag{7}$$

For the 32-node solid element of rectangular parallelepiped geometry or the 16-node degenerate solid-shell element of flat rectangular geometry, the strain vector $\bar{\varepsilon}$ is at most bicubic in ξ and η and linear in ζ. Assuming the lower-order independent strain vector ε_L to be biquadratic in ξ and η and linear in ζ for the present elements, the first, second, and fourth integrals in Eq. (7) can be integrated by $3 \times 3 \times 2$-point Gaussian quadrature rule with two points used in the ζ direction. The remaining terms are integrated by the $4 \times 4 \times 2$-point rule. Even though these integration rules hold only for the rectangular parallelepiped element or the flat rectangular element, they will be used even for the elements of arbitrary geometry in the present formulation.

According to the equivalence between the assumed strain and the displacement-dependent strain as discussed in Refs. 13, 24, and 25, it is possible to choose ε_L such that

$$\varepsilon_L = \bar{\varepsilon} \tag{8}$$

at the $3 \times 3 \times 2$ lower-order integration points. Then, applying the integration rules and the equivalence given in Eq. (8),

π_R in Eq. (7) is written as

$$\pi_R = \sum_e \left(\frac{1}{2} \int_L \bar{\varepsilon}^T C \bar{\varepsilon} \, dV_e + \int_H \varepsilon_H^T C \bar{\varepsilon} \, dV_e - \int_L \varepsilon_H^T C \bar{\varepsilon} \, dV_e - \frac{1}{2} \int_H \varepsilon_H^T C \varepsilon_H \, dV_e \right) - W \tag{9}$$

where the letters L and H under the integral signs represent the $3 \times 3 \times 2$ point integration and the $4 \times 4 \times 2$ point integration, respectively.

The higher-order strain component ε_H is assumed to be, at most, bicubic in ξ and η and linear in ζ. Symbolically, it is written as

$$\varepsilon_H = P(\xi,\eta,\zeta)\alpha_e \tag{10}$$

where $\boldsymbol{P}$ is the shape function matrix of the higher-order assumed strain and α_e is the vector of the higher-order assumed strain parameters.

Introducing Eqs. (5) and (10) into Eq. (9), the functional π_R is rewritten as

$$\pi_R = \sum_e \left(\frac{1}{2} q_e^T K_L q_e + \alpha_e^T G q_e - \frac{1}{2} \alpha_e^T H \alpha_e - q_e^T Q_e \right) \tag{11}$$

where

$$K_L = \int_L B^T C B \, dV_e \tag{12}$$

$$G = \int_H P^T C B \, dV_e - \int_L P^T C B \, dV_e \tag{13}$$

$$H = \int_H P^T C P \, dV_e \tag{14}$$

and Q_e is the element load vector.

Setting $\delta \pi_R = 0$ with respect to α_e leads to the following compatibility equation in discretized form between the higher-order assumed strain parameters and the element nodal degrees of freedom vector:

$$\alpha_e = H^{-1} G q_e \tag{15}$$

Substituting Eq. (15) into Eq. (11), the expression for π_R is written as

$$\pi_R = \sum_e \left(\frac{1}{2} q_e^T K_e q_e - q_e^T Q_e \right) \tag{16}$$

The element stiffness matrix K_e is expressed as

$$K_e = K_L + K_S \tag{17}$$

where K_S is given by

$$K_S = G^T H^{-1} G \tag{18}$$

In Eq. (17), the first term K_L, which is expressed in Eq. (12), is the element stiffness matrix of the assumed displacement model with the $3 \times 3 \times 2$ point reduced integration rule. The K_L matrix has the spurious kinematic modes, which will be shown in the next section. In the present formulation, this kinematic modes are suppressed by the K_S matrix with a carefully chosen set of higher-order strain components. Accordingly, the K_S matrix plays the role of a stabilization matrix. It should be noted that the present formulation does not require a parameter in introducing the stabilization matrix or some orthogonality conditions for the higher-order assumed strain field, while the stabilization scheme in Refs. 3-5 requires such a parameter or condition.

Note that, as shown in Eqs. (12) and (13), it is necessary to evaluate the B matrix at the two sets of integration points for generation of element stiffness matrix. In Refs. 21 and 22, the B matrix at the lower-order integration points was interpolated from the B matrix evaluated at the higher-order integration points. However, this interpolation scheme is not adopted in the present paper since it does not lead to savings in computing time.

III. Kinematic Modes and Higher-Order Assumed Strain

For the spurious kinematic modes of the K_L matrix,

$$\bar{\varepsilon} = 0 \tag{19}$$

at the $3 \times 3 \times 2$ integration points. Using Eq. (19), the kinematic modes can be determined analytically for a three-dimensional solid element with regular parallelepiped geometry and a degenerate solid-shell element with flat rectangular shape geometry.

A. Three-Dimensional Solid Element with 32 Nodes

When the global and the local coordinate systems coincide with each other, the displacement component u for a cubic element with sides along $x = \pm 1$, $y = \pm 1$, and $z = \pm 1$ may be written as

$$\begin{aligned} u = {} & a_1 + a_2 x + a_3 y + a_4 x^2 + a_5 xy + a_6 y^2 + a_7 x^3 + a_8 x^2 y \\ & + a_9 xy^2 + a_{10} y^3 + a_{11} x^3 y + a_{12} x^2 y^2 + a_{13} xy^3 + a_{14} x^3 y^2 \\ & + a_{15} x^2 y^3 + a_{16} x^3 y^3 + z(b_1 + b_2 x + b_3 y + b_4 x^2 + b_5 xy \\ & + b_6 y^2 + b_7 x^3 + b_8 x^2 y + b_9 xy^2 + b_{10} y^3 + b_{11} x^3 y \\ & + b_{12} x^2 y^2 + b_{13} xy^3 + b_{14} x^3 y^2 + b_{15} x^2 y^3 + b_{16} x^3 y^3) \end{aligned} \tag{20}$$

and the other two components v and w can be similarly expressed. Note that u, v, and w are displacements in the x, y, and z directions, respectively. Using these expressions for displacements, Eq. (19) leads to 108 homogeneous equations with 96 unknown parameters. Solving these equations gives the displacement fields that produce zero strain. Excluding the rigid body modes, the spurious kinematic modes are identified as follows:

$$u = c_1 y(3x^2 + y^2 - 5x^2y^2); \quad v = -c_1 x(x^2 + 3y^2 - 5x^2y^2) \tag{21}$$

$$u = c_2 yz(3 - 15x^2 - 5y^2 + 25x^2y^2);$$

$$v = -c_2 xz(3 - 5x^2 - 15y^2 + 25x^2y^2) \tag{22}$$

$$u = c_3 xy(9 - 15x^2 - 15y^2 + 25x^2y^2) \tag{23}$$

$$v = c_4 xy(9 - 15x^2 - 15y^2 + 25x^2y^2) \tag{24}$$

$$w = c_5 xy(9 - 15x^2 - 15y^2 + 25x^2y^2) \tag{25}$$

$$u = c_6 xyz(9 - 15x^2 - 15y^2 + 25x^2y^2) \tag{26}$$

$$v = c_7 xyz(9 - 15x^2 - 15y^2 + 25x^2y^2) \tag{27}$$

$$w = c_8 xyz(9 - 15x^2 - 15y^2 + 25x^2y^2) \tag{28}$$

where $c_1,\ldots,c_8$ are arbitrary constants. Among the above eight spurious kinematic modes, the modes in Eqs. (21) and (22) are incompatible and disappear for an assembly of only two elements. All other modes are compatible and may result in an unstable finite element even after assembly of elements. In the present formulation, these compatible modes are to be suppressed by properly choosing higher-order strain terms.

The strain terms corresponding to the compatible kinematic modes in Eqs. (23–28) are given by

$$\bar{\varepsilon}_{xx} = (9y - 45x^2y - 15y^3 + 75x^2y^3)(c_3 + c_6 z) \tag{29}$$

$$\bar{\varepsilon}_{yy} = (9x - 15x^3 - 45xy^2 + 75x^3y^2)(c_4 + c_7 z) \tag{30}$$

$$\bar{\varepsilon}_{zz} = c_8(9xy - 15x^3y - 15xy^3 + 25x^3y^3) \tag{31}$$

$$\bar{\varepsilon}_{xy} = (9x - 15x^3 - 45xy^2 + 75x^3y^2)(c_3 + c_6 z) + (9y - 45x^2y - 15y^3 + 75x^2y^3)(c_4 + c_7 z) \tag{32}$$

$$\bar{\varepsilon}_{yz} = c_7(9xy - 15x^3y - 15xy^3 + 25x^3y^3) + (9x - 15x^3 - 45xy^2 + 75x^3y^2)(c_5 + c_8 z) \tag{33}$$

$$\bar{\varepsilon}_{zx} = c_6(9xy - 15x^3y - 15xy^3 + 25x^3y^3) + (9y - 45x^2y - 15y^3 + 75x^2y^3)(c_5 + c_8 z) \tag{34}$$

These equations provide a basis for selecting higher-order assumed strain terms. For example, the kinematic mode associated with c_3 can be suppressed by including either x^2y^3 in ε^H_{xx} or x^3y^2 in ε^H_{xy}, where the superscript H represents the higher-order strain component. The kinematic mode corresponding to c_5 is suppressed by including either the x^3y^2 term in ε^H_{yz} or the x^2y^3 term in ε^H_{zx}. In the present formulation, both terms are included in the assumed strain components to avoid a directional imbalance to the element stiffness matrix. Therefore, more than one choice of higher-order assumed strain field can be employed to suppress the compatible kinematic modes. However, the number of assumed strain terms independent of the z coordinate should be minimized to avoid locking.[13,21]

With these considerations, we may choose the following higher-order strain field for the three-dimensional 32-node solid element:

$$\varepsilon^H_{xx} = 0; \quad \varepsilon^H_{yy} = 0; \quad \varepsilon^H_{zz} = 0 \tag{35a}$$

$$\varepsilon^H_{xy} = \alpha_1 x^2y^3 + \alpha_2 x^3y^2 + \alpha_3 zx^2y^3 + \alpha_4 zx^3y^2 \tag{35b}$$

$$\varepsilon^H_{yz} = \alpha_5 x^3y^2 + \alpha_6 zx^3y^2; \quad \varepsilon^H_{zx} = \alpha_7 x^2y^3 + \alpha_8 zx^2y^3 \tag{35c}$$

where $\alpha_1, \alpha_2, \ldots, \alpha_8$ are unknown parameters. The size of P matrix in Eq. (10) is 6×8. In this assumed strain version, referred to as A1, the polynomial terms in ε^H_{xy} suppress the kinematic modes related to c_3, c_4, c_6, and c_7. The terms in ε^H_{yz} or in ε^H_{zx} suppress the remaining kinematic modes associated with c_5 and c_8.

Noting that the mode associated with c_8 can be suppresssed by including x^3y^3 in ε^H_{zz}, another version of the higher-order assumed strain field is obtained as follows:

$$\varepsilon^H_{xx} = 0; \quad \varepsilon^H_{yy} = 0; \quad \varepsilon^H_{zz} = \alpha_1 x^3y^3 \tag{36a}$$

$$\varepsilon^H_{xy} = \alpha_2 x^2y^3 + \alpha_3 x^3y^2 + \alpha_4 zx^2y^3 + \alpha_5 zx^3y^2 \tag{36b}$$

$$\varepsilon^H_{yz} = \alpha_6 x^3y^2; \quad \varepsilon^H_{zx} = \alpha_7 x^2y^3 \tag{36c}$$

This set, called the A2 version, has seven unknown parameters, resulting in a 6×7 P matrix. In this version, the kinematic mode associated with c_5 is suppressed by x^3y^2 in ε^H_{yz} or x^2y^3 in ε^H_{zx}.

The compatible kinematic modes corresponding to c_3, c_4, c_6, and c_7 can also be suppressed by the following set of higher-order assumed strain field:

$$\varepsilon^H_{xx} = \alpha_1 x^2y^3 + \alpha_2 zx^2y^3; \quad \varepsilon^H_{yy} = \alpha_3 x^3y^2 + \alpha_4 zx^3y^2 \tag{37a}$$

$$\varepsilon^H_{zz} = 0; \quad \varepsilon^H_{xy} = 0 \tag{37b}$$

$$\varepsilon^H_{yz} = \alpha_5 x^3y^2 + \alpha_6 zx^3y^2; \quad \varepsilon^H_{zx} = \alpha_7 x^2y^3 + \alpha_8 zx^2y^3 \tag{37c}$$

In this version, designated B1, the higher-order polynomial terms in ε^H_{xx} suppress the modes represented by c_3 and c_6. On the other hand, the terms in ε^H_{yy} suppress the modes associated with c_4 and c_7. The remaining modes are suppressed by the terms in either ε^H_{yz} or ε^H_{zx}.

Alternatively, the following set of the higher-order strain field, referred to as B2, can be used to suppress the compatible kinematic modes:

$$\varepsilon^H_{xx} = \alpha_1 x^2y^3 + \alpha_2 zx^2y^3; \quad \varepsilon^H_{yy} = \alpha_3 x^3y^2 + \alpha_4 zx^3y^2 \tag{38a}$$

$$\varepsilon^H_{zz} = \alpha_5 x^3y^3; \quad \varepsilon^H_{xy} = 0 \tag{38b}$$

$$\varepsilon^H_{yz} = \alpha_6 x^3y^2; \quad \varepsilon^H_{zx} = \alpha_7 x^2y^3 \tag{38c}$$

For an element with an arbitrary curved, irregular shape geometry, the higher-order assumed strain components are chosen by replacing x, y, and z in Eqs. (35–38) with the parent or natural coordinates ξ, η, and ζ, respectively. For example, the higher-order assumed strain ε^H_{xy} in Eq. (35b) is replaced with

$$\varepsilon^H_{xy} = \alpha_1 \xi^2\eta^3 + \alpha_2 \xi^3\eta^2 + \alpha_3 \zeta\xi^2\eta^3 + \alpha_4 \zeta\xi^3\eta_2$$

Other strain components are similarly expressed. Then, the higher-order assumed strain fields selected in this manner consist of incomplete polynomial sets in ξ and η. For an element with an arbitrary shape geometry, this leads to an element stiffness matrix which is, in general, not invariant. The invariance of an element stiffness matrix is enforced by assigning a specific orthogonal local coordinate system at each integration point for a given element geometry.[17] As shown in Fig. 3, two unit vectors $\boldsymbol{v}_1$ and $\boldsymbol{v}_2$ are parallel to the parent coordinates ξ, η and the unit vector $\boldsymbol{v}_m$ bisects $\boldsymbol{v}_1$ and $\boldsymbol{v}_2$. The unit vectors $\boldsymbol{a}_1$, $\boldsymbol{a}_2$, and $\boldsymbol{a}_3$ of the local coordinate system is determined as follows: First, $\boldsymbol{a}_3$ is obtained such that $\boldsymbol{a}_3 = (\boldsymbol{v}_1 \times \boldsymbol{v}_2)/\|\boldsymbol{v}_1 \times \boldsymbol{v}_2\|$. Next, the rotation of $\boldsymbol{v}_m$ around $\boldsymbol{a}_3$ by 45 deg counterclockwise gives $\boldsymbol{a}_1$. Finally, $\boldsymbol{a}_2$ is found from $\boldsymbol{a}_2 = \boldsymbol{a}_3 \times \boldsymbol{a}_1$. With this definition of unit vectors, a unique set of the local coordinate system is established at each integration point. This leads to an element stiffness matrix independent of the choice of the global coordinate system.

The element locking is determined by the z- or ζ-independent terms in the assumed strain components of ε^H_{xx}, ε^H_{yy}, ε^H_{xy}, ε^H_{yz}, and ε^H_{zx}. The ε^H_{zz} component plays no role in the element locking. Thus the A1 version element and the A2 version element are expected to exhibit a similar element locking behavior because, excluding ε^H_{zz}, they have the identical ζ-independent terms in the assumed strain field. Similarly, the B1 version and the B2 version will exhibit almost identical element locking characteristics. On the other hand, the A version

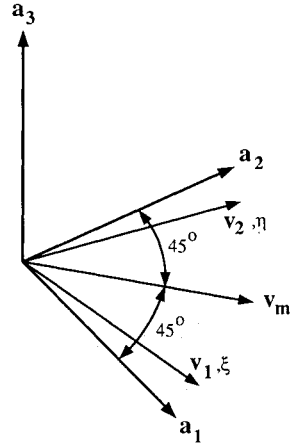

Fig. 3 Three orthogonal unit vectors a_1, a_2, and a_3 of a local coordinate system.

models (M32A1 and M32A2) and the B version models (M32B1 and M32B2) for the present three-dimensional solid element utilize different higher-order assumed strain terms in ε_{xx}^H, ε_{yy}^H, and ε_{xy}^H. Therefore, for curved shells, the two versions could exhibit a different degree of inplane or membrane locking.

B. Degenerate Solid Shell Element with 16 Nodes

Expressing translational displacements u, v, and w and rotational angles θ_1 and θ_2 as polynomial functions in x and y, we can obtain the analytical expressions for the spurious kinematic modes of the flat rectangular element with sides $x = \pm 1$ and $y = \pm 1$ by applying Eq. (19). As shown in Ref. 22, the kinematic modes are as follows:

$$u = d_1 y(3x^2 + y^2 - 5x^2y^2); \quad v = -d_1 x(x^2 + 3y^2 - 5x^2y^2) \tag{39}$$

$$\theta_1 = d_2 x(3 - 5x^2 - 15y^2 + 25x^2y^2);$$

$$\theta_2 = d_2 x(3 - 15x^2 - 5y^2 + 25x^2y^2) \tag{40}$$

$$u = d_3 xy(9 - 15x^2 - 15y^2 + 25x^2y^2) \tag{41}$$

$$v = d_4 xy(9 - 15x^2 - 15y^2 + 25x^2y^2) \tag{42}$$

$$w = d_5 xy(9 - 15x^2 - 15y^2 + 25x^2y^2) \tag{43}$$

$$\theta_1 = d_6 xy(9 - 15x^2 - 15y^2 + 25x^2y^2) \tag{44}$$

$$\theta_2 = d_7 xy(9 - 15x^2 - 15y^2 + 25x^2y^2) \tag{45}$$

Among the above kinematic modes, the modes in Eqs. (39) and (40) need not be suppressed at an element level since they are incompatible and disappear for an assembly of only two elements. The remaining modes are compatible and are suppressed by the higher-order assumed strain terms.

Following a similar argument given in the 32-node solid element case, the following set of the higher-order assumed strain field, the A version, can be used to suppress the compatible kinematic modes in Eqs. (41) to (45):

$$\varepsilon_{xx}^H = 0; \quad \varepsilon_{yy}^H = 0 \tag{46a}$$

$$\varepsilon_{xy}^H = \alpha_1 x^2y^3 + \alpha_2 x^3y^2 + \alpha_3 zx^2y^3 + \alpha_4 zx^3y^2 \tag{46b}$$

$$\varepsilon_{yz}^H = \alpha_5 x^3y^2; \quad \varepsilon_{zx}^H = \alpha_7 x^2y^3 \tag{46c}$$

In this set, the higher-order terms in ε_{xy}^H suppress the kinematic modes related to d_3, d_4, d_6, and d_7. The term in either ε_{yz} or ε_{zx} suppresses the mode represented by d_5.

An alternative choice, the B version, is given as

$$\varepsilon_{xx}^H = \alpha_1 x^2y^3 + \alpha_2 zx^2y^3; \quad \varepsilon_{yy}^H = \alpha_3 x^3y^2 + \alpha_4 zx^3y^2 \tag{47a}$$

$$\varepsilon_{xy}^H = 0 \tag{47b}$$

$$\varepsilon_{yz}^H = \alpha_5 x^3y^2; \quad \varepsilon_{zx}^H = \alpha_7 x^2y^3 \tag{47c}$$

This B version of the higher-order assumed strain was investigated in Ref. 22. In this version, the compatible kinematic modes associated with d_3, d_4, d_6, and d_7 are suppressed by the terms in ε_{xx}^H and ε_{yy}^H.

For an element with arbitrary geometry, the higher-order assumed strains and the local coordinate system are chosen in the manner described previously for the 32-node solid element. Note that the A version element (M16A) and the B version element (M16B) have different polynomial terms in ε_{xx}^H, ε_{yy}^H, and ε_{xy}^H. For curved shells, this difference could manifest itself as a different degree of membrane locking.

IV. Numerical Tests

Simple benchmark example problems were used to test the performance of the present finite-element models with the different sets of the higher-order assumed strain field. Numerical results are compared with analytical or other independent solutions. All computations were performed in double precision on the Sun Microsystems machine at the University of Maryland. The present numerical examples do not address the results of the patch test. However, these results will be the subject of a forthcoming paper.

A. Comparison of Computing Time

In order to evaluate computing efficiency, a test was run in which the stiffness matrix of a single element was computed 25 times consecutively. The test result shows that for the 16-node degenerate solid-shell element, the computing time for the present formulation is only about 30% of that of the conventional mixed model and about 78% of that of the assumed displacement element with the $4 \times 4 \times 2$ point integration rule. A similar result was obtained for the 32-node three-dimensional solid element. Clearly, the present mixed formulation is far more efficient than the conventional mixed formulation.

B. Clamped Square Plate Under a Uniform Pressure

A clamped plate is a good example problem to investigate the degree of transverse shear locking for a finite-element model. Due to symmetry in geometry and loading, a quarter plate was used for modeling. Three uniformly divided 1×1, 2×2, and 3×3 meshes and two distorted meshes, 2×2D and 3×3D as shown in Figs. 4a and 4b, were tested for the length to thickness (L/t) ratios of 10^2, 10^3, and 10^4. Elastic constants used here are $E = 10^7$ psi and $\nu = 0.3$.

Table 1 lists the numerical values of the central deflection normalized with respect to the analytical solution obtained from thin-plate theory.[26] The 32-node solid-element models produce very accurate solutions for the L/t ratios of 10^2 and 10^3. For the $L/t = 10^4$ case, the 32-node solid element shows slightly the effect of transverse shear locking. However, this value of L/t ratio is beyond the practical range. For $L/t = 10^2$ and 10^3, there is no difference among the different versions of the 32-node element. This appears due to the fact that all versions have the same ζ-independent terms in the higher-order assumed strain components ε_{yz}^H and ε_{zx}^H. For $L/t = 10^4$, there are some differences among them.

The 16-node degenerate solid elements (M16A and M16B) based on the present mixed formulations do not exhibit any transverse shear locking regardless of mesh distortion and the L/t ratios. As expected, M16A and M16B gave identical results since both A and B versions have the same terms in the assumed ε_{yz}^H and ε_{zx}^H. The 16-node degenerate solid-shell element based on the assumed displacement method, referred to as D16 in this paper, gives numerical results close to the analytical solution for the uniform regular meshes. However, for the 2×2D mesh, the performance of D16 element deteriorates as the plate becomes thin. Although the performance is improved with the 3×3D mesh, the D16 solution is still about 8% lower than the analytical solution for $L/t = 10^4$.

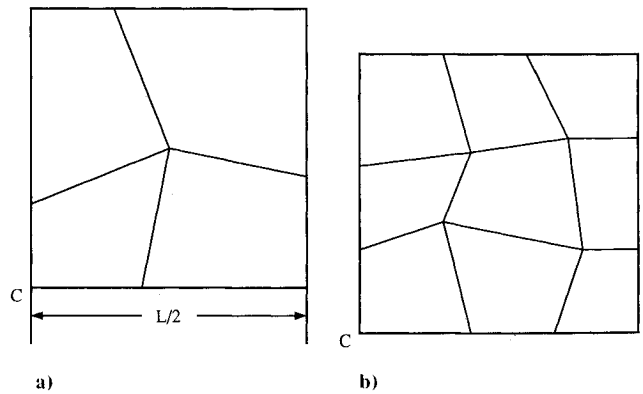

Fig. 4 Two distorted meshes for a clamped plate: a) 2×2 mesh; and b) 3×3 mesh.

Table 1 Normalized maximum deflection of the clamped square plate

L/t	Mesh	M32A1,M32A2	M32B1,M32B2	M16A,M16B	D16
10^2	1 × 1	0.9961	0.9961	0.9965	1.0482
	2 × 2	1.0018	1.0018	1.0021	1.0016
	3 × 3	1.0019	1.0019	1.0022	1.0002
	2 × 2D	1.0021	1.0021	1.0024	0.9945
	3 × 3D	1.0018	1.0018	1.0021	1.0013
10^3	1 × 1	0.9945	0.9945	0.9945	1.0474
	2 × 2	1.0002	1.0002	1.0002	1.0000
	3 × 3	1.0003	1.0003	1.0003	1.0000
	2 × 2D	0.9959	0.9959	0.9969	0.9486
	3 × 3D	0.9995	0.9995	0.9996	0.9978
10^4	1 × 1	1.0281	1.0234	0.9945	1.0474
	2 × 2	0.9779	0.9680	1.0001	1.0000
	3 × 3	1.0063	1.0128	1.0002	1.0000
	2 × 2D	0.9598	0.9630	0.9713	0.3007
	3 × 3D	0.9765	0.9788	0.9979	0.9173

Table 2 Normalized maximum deflection of the pinched circular ring

R/t	Mesh	M32A1	M32A2	M32B1	M32B2	M16A	M16B	D16
60	2	0.9990	0.9990	0.9768	0.9768	0.9993	0.9766	0.7405
	3	1.0002	1.0002	0.9975	0.9975	1.0002	0.9975	0.9051
100	2	0.9988	0.9988	0.9467	0.9467	0.9991	0.9457	0.7298
	3	1.0000	1.0000	0.9928	0.9928	0.9999	0.9928	0.8885
500	2	0.9987	0.9987	0.8059	0.8059	0.9990	0.7994	0.7233
	3	0.9999	0.9999	0.9298	0.9297	0.9998	0.9292	0.8769
1000	2	0.9989	0.9987	0.7879	0.7878	0.9989	0.7803	0.7224
	3	0.9990	0.9994	0.9022	0.9022	0.9998	0.9020	0.8763

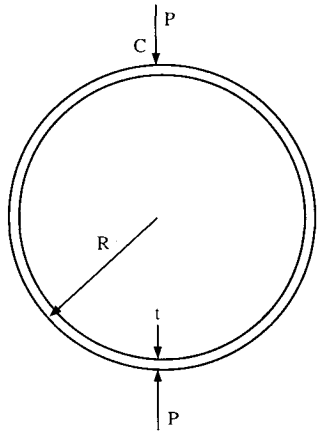

Fig. 5 A pinched circular ring.

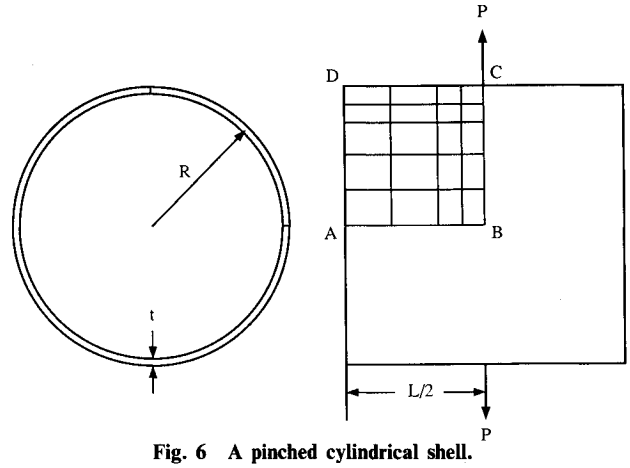

Fig. 6 A pinched cylindrical shell.

C. Pinched Circular Ring

As shown in Fig. 5, two concentrated loads (P) are applied to the opposite sides of the ring. Utilizing the symmetrical conditions, equally divided two- and three-element mesh were used to model a quarter of the ring. Four values of R/t ratio, 60, 100, 500, and 1000, were considered here. Again, elastic constants were $E = 10^7$ psi and $v = 0.3$.

Table 2 lists the nondimensional deflection at the load point normalized to the analytical solution.[13] With only two elements, the M32A1, M32A2, and the M16A models give highly accurate numerical results over the range of R/t ratios tested here. On the other hand, the elements with the type B assumed strain (M32B1, M32B2, and M16B) need more refined meshes than the previous models to obtain satisfactory numerical solutions. As R/t increases, the B-version models converge even more slowly than the A-version elements. As expected, for the 32-node element, there is little difference between the A1 and A2 versions. Similarly, B1 and B2 versions of the 32-node element are very close to each other. For all R/t ratios, the D16 element shows poorer performance than either the A or B version elements. The D16 model exhibits symptoms of locking as the ring becomes thinner.

D. Pinched Cylindrical Shell with Diaphragmed Ends

Figure 6 depicts a cylindrical shell under two opposite points load (P) on the circle at the midsection. Both ends of the cylinder are diaphragmed. The radius of the cylinder, R, is 4.953 in. and the length $L = 2R$. Elastic constants are $E = 1.05 \times 10^7$ psi and $v = 0.3$. Due to geometric and loading symmetry, only one octant of the cylinder was modeled by

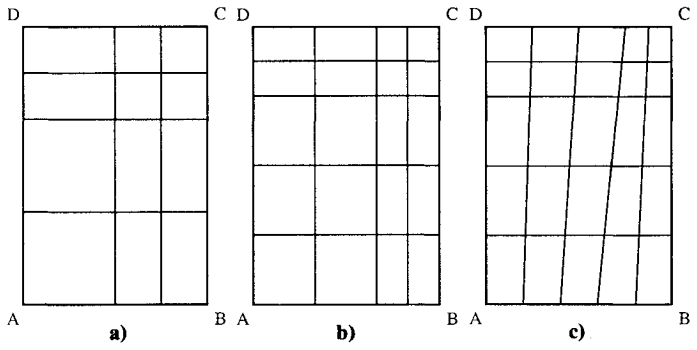

Fig. 7 Meshes for the pinched cylindrical shell: a) 3 × 4 mesh; b) 4 × 5 mesh; and c) 5 × 6 mesh.

Table 3 Nondimensional deflection at load point $C(-EtW_C/P)$ of the pinched cylinder

		Mesh			
R/t	Element	3 × 4	4 × 5	5 × 6	Analytical
100	M32A1	165.7	166.8	167.1	164.3
	M32A2	165.2	166.5	167.0	
	M32B1	165.4	166.7	167.1	
	M32B2	165.0	166.4	166.9	
	M16A	165.2	166.0	166.3	
	M16B	165.0	166.1	166.4	
	D16	131.1	151.2	159.1	
300	M32A1	637.4	643.6	647.6	647.3
	M32A2	628.4	641.1	646.7	
	M32B1	631.5	640.2	646.0	
	M32B2	622.5	637.7	645.1	
	M16A	637.0	643.2	647.2	
	M16B	631.5	639.7	645.6	
	D16	322.7	444.0	530.8	
500	M32A1	1197.8	1204.6	1215.4	1223.4
	M32A2	1160.3	1192.2	1211.2	
	M32B1	1161.2	1192.7	1206.6	
	M32B2	1123.4	1180.2	1202.3	
	M16A	1197.5	1204.5	1215.5	
	M16B	1162.6	1192.2	1206.4	
	D16	422.8	675.1	846.8	

Table 4 Nondimensional deflection at point $A(-Dw_A/PR^2)$ of the hemisphere

		Number of elements			
R/t	Element	4	9	16	Analytical
250	M32A1	0.178	0.185	0.185	0.185
	M32A2	0.170	0.184	0.185	
	M32B1	0.174	0.183	0.185	
	M32B2	0.169	0.182	0.184	
	M16A	0.175	0.185	0.185	
	M16B	0.172	0.183	0.185	
	D16	0.028	0.113	0.160	
500	M32A1	0.165	0.182	0.183	–
	M32A2	0.141	0.181	0.183	
	M32B1	0.161	0.177	0.181	
	M32B2	0.152	0.177	0.181	
	M16A	0.153	0.181	0.183	
	M16B	0.157	0.177	0.181	
	D16	0.008	0.054	0.123	

two regular 3 × 4 and 4 × 5 meshes as shown in Figs. 7a and 7b and one irregular 5 × 6 mesh illustrated in Fig. 7c. Small size elements were employed in the vicinity of the load point C where the steep gradient of deflection is expected.

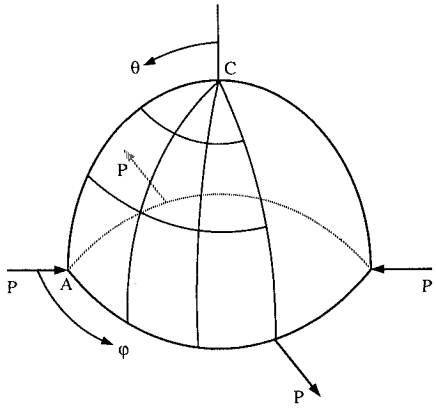

Fig. 8 A hemispherical shell subjected to alternating concentrated loads.

Table 3 reports the nondimensional deflection at the load point of the cylinder for R/t ratios of 100, 300, and 500. Analytical solutions based on a shell theory that neglects the effect of transverse shear strain are given by Flügge.[27] For the $R/t = 100$ case, the present elements with the A version or the B version assumed strain field give numerical values very close to the analytical solutions regardless of mesh types. For $R/t = 500$, M32A1, M32A2, and M16A elements show slightly faster convergence than M32B1, M32B2, and M16B, respectively. In the cases of $R/t = 300$ and 500 with the 3 × 4 mesh, the M32A1 or the M32B1 model is slightly better than the M32A2 or the M32B2 model, respectively. On the other hand, D16 shows the effect of locking. Its performance deteriorates as R/t ratio increases.

E. Hemisphere under Alternating Point Loads

Figure 8 shows a hemispherical shell subjected to alternating concentrated loads (P) at its free edge. The radius (R) is 1.0 in. and elastic constants are $E = 10^7$ psi and $\nu = 0.3$. Again, symmetry conditions permit modeling the problem with only a quarter of the hemisphere. For ease of modeling, a small segment within 0.5 deg of the point C was excluded, and the proper boundary conditions were applied along the cut edge. Meshes with 4, 9, and 16 elements were generated by dividing the shell structure uniformly over the angles θ and φ.

In Table 4, the computed nondimensional deflection $-Dw_A/PR^2$ is listed. The symbol D represents bending rigidity, and w_A is the normal deflection of the point A of the hemisphere. Numerical results for R/t ratios of 250 and 500 are given in the table. The analytical solution for the $R/t = 250$ case was reported by Morley and Morris.[28] For $R/t = 250$, the solutions for the 16-element mesh of all present elements agree with the analytical solution. Again, for both R/t ratios, the mixed models with the B version assumed strain shows slower convergence than those with the A version assumed strain. For the four-element mesh, the M32A2 element produced lower solutions than the M32A1 element especially for $R/t = 500$. However, as the element number of

meshes increased, both models gave almost identical results. As is the case for the pinched cylindrical shell, the D16 model shows severe effects of locking, especially for the $R/t = 500$ case.

V. Conclusions

In the present mixed formulation, the assumed independent strain field is split into a lower-order part and a higher-order part. This leads to a substantial saving in computing time needed to generate an element stiffness matrix. As the computing time comparison test indicates, the present formulation requires much less time to evaluate the element stiffness matrix than the conventional mixed formulation and less time than even the assumed displacement model with the $4 \times 4 \times 2$ point integration.

The higher-order assumed strain field is chosen to suppress only compatible spurious kinematic modes, and thus the resulting elements are kinematically unstable at element level. However, the unsuppressed kinematic modes are incompatible and disappear with an assembly of only two elements. Therefore, the present formulation leads to globally stable finite-element models.

For the 32-node solid element, four sets of the higher-order assumed strain field were tested. Among these, A1 and A2 versions are essentially equivalent to each other as far as locking is concerned since they share the same z or ζ-independent terms in ε^H_{xx}, ε^H_{yy}, ε^H_{xy}, ε^H_{yz}, and ε^H_{xz} components. Similarly, B1 and B2 versions are equivalent to each other. The A version and the B version are different in that they use different terms in ε^H_{xx}, ε^H_{yy}, and ε^H_{xy}. The numerical tests essentially support these observations. The pinched ring problem demonstrates the marked difference between the A version and the B version assumed strains. However, the other shell problems show much less difference. For the 16-node element, similar observations are made regarding the difference between the A version and the B version assumed strains. All in all, the A version assumed strain appears to be better than the B version for both the 16-node degenerate solid-shell element and the 32-node three-dimensional solid element.

The present higher-order elements are free of locking and kinematically stable when assembled. Therefore, they can be used for the analysis of shell structures with a high degree of confidence. Moreover, they can provide benchmark solutions against which other lower-order finite elements can be tested. In the near future, the present formulation will be extended to geometrically nonlinear isotropic and composite shells.

Acknowledgment

The present work was supported by the Office of Naval Research (N00014-84-K-0385).

References

[1]Pugh, E. D. L., Hinton, E., and Zienkiewicz, O. C., "A Study of Quadrilateral Plate Bending Elements with Reduced Integration," *International Journal for Numerical Methods in Engineering*, Vol. 12, No. 7, 1978, pp. 1059–1079.

[2]Parish, H., "A Critical Survey of the 9-Node Degenerate Shell Element with Special Emphasis on Thin Shell Application and Reduced Integration," *Computer Methods in Applied Mechanics and Engineering*, Vol. 20, No. 3, 1979, pp. 323–350.

[3]Belytschko, T., Ong, J. S. J., and Liu, W. K., "A Consistent Control of Spurious Singular Modes in the 9-Node Largrange Element for the Laplace and Mindlin Plate Equations," *Computer Methods in Applied Mechanics and Engineering*, Vol. 44, No. 3, 1984, pp. 269–295.

[4]Belytschko, T., Liu, W. K., Ong, J. S. J., and Lam, J. S. L., "Implementation and Application of a 9-Node Lagrange Shell Element with Spurious Mode Control," *Computers and Structures*, Vol. 20, No. 1–3, 1985, pp. 121–128.

[5]Belytschko, T., and Wong, B. L., "Assumed Strain Stabilization Procedure for the 9-Node Lagrange Shell Element," *International Journal for Numerical Methods in Engineering*, Vol. 28, No. 2, 1989, pp. 385–414.

[6]Hughes, T. J. R., and Tezduyar, T. E., "Finite Elements Based upon Mindlin Plate Theory with Particular Reference to the Four-Node Isoparametric Element," *Journal of Applied Mechanics,* Vol. 48, No. 3, 1981, pp. 587–596.

[7]Bathe, K. J., and Dvorkin, E. N., "A Four-Node Plate Bending Element Based on Mindlin/Reissner Theory and a Mixed Interpolation," *International Journal for Numerical Methods in Engineering*, Vol. 21, No. 2, 1985, pp. 367–383.

[8]Park, K. C., and Stanley, G. M., "A Curved C^o Shell Element Based on Assumed Natural-Coordinate Strains," *Journal of Applied Mechanics*, Vol. 53, No. 2, 1986, pp. 278–290.

[9]Jang, J., and Pinsky, P. M., "An Assumed Covariant Strain Based 9-Node Shell Element," *International Journal for Numerical Methods in Engineering*, Vol. 24, No. 12, 1987, pp. 2389–2411.

[10]Stolarski, H. K., and Chiang, M. M., "The Mode-Decomposition, C^o Formulation of Curved, Two-Dimensional Structural Elements," *International Journal for Numerical Methods in Engineering*, Vol. 28, No. 1, 1989, pp. 145–154.

[11]Spilker, R. L., "Invariant 8-Node Hybrid Stress Elements for Thin Plates and Shells," *International Journal for Numerical Methods in Engineering*, Vol. 17, No. 8, 1982, 1153–1178.

[12]Saleeb, A. F., Chang, T. Y., and Graf, W., "A Quadrilateral Shell Element Using a Mixed Formulation," *Computers and Structures*, Vol. 26, No. 5, 1987, pp. 787–803.

[13]Lee, S. W., and Pian, T. H. H., "Improvement of Plate and Shell Finite Elements by Mixed Formulations," *AIAA Journal*, Vol. 16, No. 1, 1978, pp. 29–34.

[14]Ahmad, S., Irons, B. M., and Zienkiewicz, O. C., "Analysis of Thick and Thin Shell Structures by Curved Elements," *International Journal for Numerical Methods in Engineering*, Vol. 2, No. 3, 1970, pp. 419–451.

[15]Lee, S. W., Wong, S. C., and Rhiu, J. J., "Study of a Nine-Node Mixed Formulation Finite Element for Thin Plates and Shells," *Computers and Structures*, Vol. 21, No. 6, 1985, pp. 1325–1334.

[16]Rhiu, J. J., and Lee, S. W., "A Nine Node Finite Element for Analysis of Geometrically Non-Linear Shells," *International Journal for Numerical Methods in Engineering*, Vol. 26, No. 9, 1988, pp. 1945–1962.

[17]Yeom, C. H., and Lee, S. W., "An Assumed Strain Finite Element Model for Large Deflection Composite Shells," *International Journal for Numerical Methods in Engineering*, Vol. 28, No. 8, 1989, pp. 1749–1768.

[18]Kim, Y. H., and Lee, S. W., "A Solid Element Formulation for Large Deflection Analysis of Composite Shell Structures," *Computers and Structures*, Vol. 30, No. 1/2, 1988, pp. 269–274.

[19]Russell, R. M., "Finite Element Analysis of Shells with a Thirty-Two Node, Three-Dimensional, Solid Element Based on the Assumed Strain Formulation," M.S. Thesis, Univ. of Maryland, 1988.

[20]Lee, S. W., and Rhiu, J. J., "A New Efficient Approach to the Formulation of Mixed Finite Element Models for Structural Analysis," *International Journal for Numerical Methods in Engineering*, Vol. 23, No. 9, 1986, pp. 1629–1641.

[21]Rhiu, J. J., and Lee, S. W., "A New Efficient Mixed Formulation for Thin Shell Finite Element Models," *International Journal for Numerical Methods in Engineering*, Vol. 24, No. 3, 1987, pp. 581–604.

[22]Rhiu, J. J., and Lee, S. W., "A Sixteen Node Shell Element with a Matrix Stabilization Scheme," *Computational Mechanics*, Vol. 3, No. 2, 1988, pp. 99–113.

[23]Ausserer, M. F., and Lee, S. W., "An Eighteen-Node Solid Element for Thin Shell Analysis," *International Journal for Numerical Methods in Engineering*, Vol. 26, No. 6, 1988, pp. 1345–1364.

[24]Lee, S. W., "Finite Element Methods for Reduction of Constraints and Creep Analysis," Ph.D. Dissertation, Massachusetts Inst. of Technology, Cambridge, MA, 1978.

[25]Malkus, D. S., and Hughes, T. J. R., "Mixed Finite Element Methods-Reduced and Selective Integration Techniques: A Unification of Concepts," *Computer Methods in Applied Mechanics and Engineering*, Vol. 15, No. 1, 1978, pp 63–81.

[26]Timoshenko, S. P., and Woinowsky-Krieger, S., *Theory of Plates and Shells*, 2nd ed., McGraw-Hill, New York, 1959.

[27]Flügge, W., *Stresses in Shells*, Springer-Verlag, Berlin, 1962.

[28]Morley, L. S. D., and Morris, A. J., "Conflict Between Finite Elements and Shell Theory," *Finite Element Methods in the Commercial Environment,* edited by J. Robinson, Vol. 2, Okehampton, UK, 1978.